Check for updates

Self-buckling and self-writhing of semi-flexible microorganisms†

Wilson Lough, [ID] *[a] Douglas B. Weibel[b] and Saverio E. Spagnolie[cd]

The twisting and writhing of a cell body and associated mechanical stresses is an underappreciated constraint on microbial self-propulsion. Multi-flagellated bacteria can even buckle and writhe under their own activity as they swim through a viscous fluid. New equilibrium configurations and steady-state dynamics then emerge which depend on the organism's mechanical properties and on the oriented distribution of flagella along its surface. Modeling the cell body as a semi-flexible Kirchhoff rod and coupling the mechanics to a flagellar orientation field, we derive the Euler–Poincaré equations governing the dynamics of the system, and rationalize experimental observations of buckling and writhing of elongated swarmer cells of the bacterium *Proteus mirabilis*. A sequence of bifurcations is identified as the body is made more compliant, due to both buckling and torsional instabilities. These studies highlight a practical requirement for the stiffness of bacteria below which self-buckling occurs and cell motility becomes ineffective.

1. Introduction

Motility introduces a number of demands on the mechanical construction of bacterial cells. Such constraints have been studied for motility organelles; slender flagella can buckle below a critical bending stiffness or above a critical motor torque,[1,2] and the same is true of the flexible flagellar hook.[3,4] The shape and size of bacterial cells is influenced by numerous considerations,[5–8] including efficient motility in liquids.[9–11] However, motile bacterial cells are canonically presumed to be rod-shaped, non-deformable structures, and cell stiffness, a feature normally provided by cell wall composition[12–14] and turgor pressure,[15] is typically overlooked in studies of motility. Cell wall stiffness regulation alters bacterial cell shape, influences motility, and enables bacteria to adapt and survive.[16,17]

The length of *Proteus mirabilis* (*P. mirabilis*) cells increases by up to 20–40× when they are in a swarming state,[18] and deformation in cell shape are visibly clear in a swarm.[19,20] *P. mirabilis* swarmer cells have reduced cell stiffness compared to normal vegetative cells.[21] Gene deletion has also been used

to artificially reduce cell stiffness.[22] But the nature and organization of any motility organelles is also important. A swarmer cell swims by rotating up to thousands of flagella which are distributed along its surface.[23,24] The flagellar motion drives active, wavelike surface features more often used to describe ciliated organisms, which themselves are classically modeled as a continuum of active stress.[25,26]

A wild-type *P. mirabilis* cell is stiff and rod-shaped and swims along a straight trajectory, with its flagella oriented with their tips opposite the swimming direction (Fig. 1e).[27] The fluid response to flagellar motion drives the body forward, and induces a rotational velocity along the long axis as dictated by the force- and torque-free nature of swimming in viscous fluids.[28] Elongated swarmer cells, however, can express a wide range of intricate and stunning dynamics. Fig. 1 shows *P. mirabilis* cells which have buckled under their own activity. The flagellar tips appear to be pointing away from the direction of local body motion, suggestive that their orientation depends upon local viscous stresses (Fig. 1a and b; see Movies M1–M4, ESI†). Strongly three-dimensional configurations and dynamics are shown in Fig. 1c, which includes a spinning motion about the direction of swimming. An even more highly deformed state with multiple self-crossings is shown in Fig. 1d.

Such active systems are particularly rich, as even passive slender bodies driven by external forces[29] or flows[30] continue to reveal new buckling behaviors.[31–36] The shapes and dynamics of elongated *P. mirabilis* cells share many similarities with active or externally forced filaments which exhibit spontaneous symmetry breaking.[37–39] The U- and S-shaped configurations in Fig. 1a and b have been observed numerically in related

[a] Department of Physics, University of Wisconsin-Madison, Madison, WI 53706, USA. E-mail: wlough@wisc.edu

[b] Department of Biochemistry, University of Wisconsin-Madison, Madison, WI 53706, USA

[c] Department of Mathematics, University of Wisconsin-Madison, 480 Lincoln Dr, Madison, WI 53706, USA

[d] Department of Chemical and Biological Engineering, University of Wisconsin-Madison, Madison, WI 53706, USA
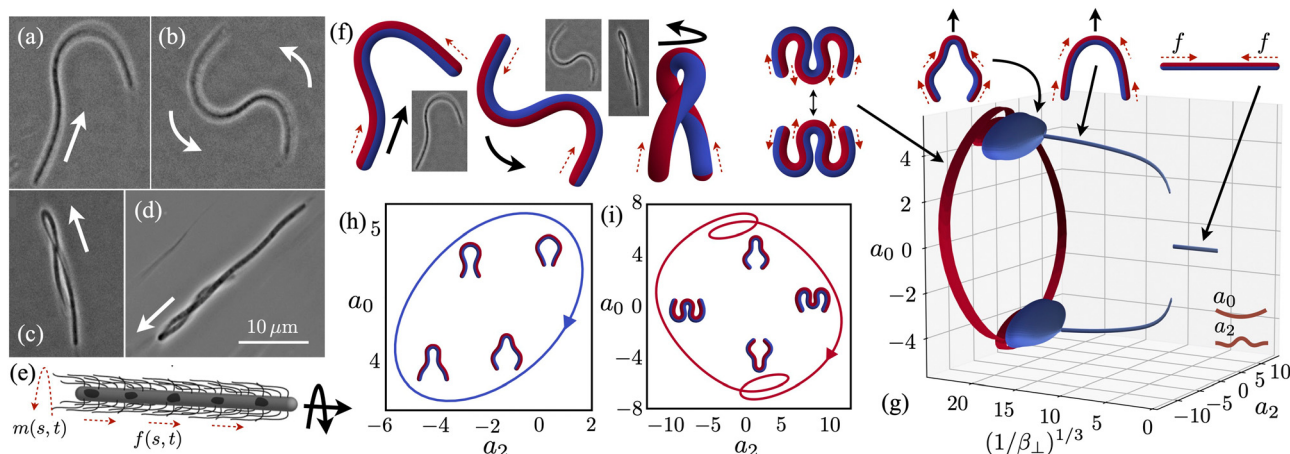
Fig. 1 (a–d) Swarmer *P. mirabilis* cells bend, rotate, and twist under their own flagellar activity (see Movies M1–M4, ESI†). Solid arrows indicate the direction of motion. (e) Flagellar stresses are modeled as a continuous force density $f(s,t)$ and proportional moment density $m(s,t)$ which drive and rotate the body through the fluid. (f) An active swimming Kirchhoff rod reproduces U-shaped swimming, S-shaped rotation, and twisted, rotating swimming states found in experiments. Dashed arrows indicate the direction of the local flagellar force and moment densities. (g) Phase diagram illustrating periodic symmetric dynamics in the absence of an active moment, $m(s,t) = 0$. The centerline curvature $\kappa(s,t) = \sum_{k=0}^{\infty} a_k(t)\phi_k(s)$ is projected onto the first two even biharmonic modes ($a_0(t)$, $a_2(t)$), and trajectories in a_0-a_2 space are plotted against $\beta_\perp^{-1/3}$, where $\beta_\perp = B_\perp/(f^*L^3)$ is a dimensionless bending stiffness, with $B_\perp$ the bending modulus, f^* a characteristic active force density, and L the body length. Bifurcations from straight filaments to swimming-U shapes, then to periodic waving-U dynamics, then to periodic flapping-W dynamics are observed as the bending stiffness is reduced. (h) A cross-section of the phase diagram in (g) with $\beta_\perp = 1.3 \times 10^{-4}$ (waving-U dynamics). (i) A cross-section of the phase diagram in (g) with $\beta_\perp = 7.6 \times 10^{-5}$ (flapping-W dynamics).

systems in two dimensions,[40] as have spiral-shaped configurations.[41] The response of semi-flexible polymers to molecular-motor-driven stress has seen tremendous interest,[42] particularly in the context of cytoskeletal networks and interphase chromatin configurations.[43–45] Flagellar propulsion, however, introduces additional features, for instance a competition between twist/bend elasticity and twist injection,[46–48] and a dynamic rearrangement of flagellar stress. It is plausible that the highly nonlinear twist-bend coupling[49,50] responsible for the emergence of writhing instabilities[51] and chiral configurations[52] in generic elastic filaments is also responsible for the configurations seen in Fig. 1c and d.

In this paper we explore numerically and analytically a Kirchhoff rod model of a long, swimming cell which is driven by active forces and moments associated with flagellar activity. The model reproduces both two- and three-dimensional configurations (Fig. 1f) and predicts microorganism buckling and writhing under its own flagellar activity and viscous stress response. Bifurcations in the shapes and dynamics appear as the cell body is made more flexible, including buckling and torsional instabilities commonly observed in passive elastic systems, and new modes of motion are found upon the introduction of the active moment.

The paper is organized as follows. In Section 2 we present the active Kirchhoff rod model, in which the deformable body dynamics are described using the Euler–Poincaré formalism.[53–55] The numerical method used to explore the system, which exploits the geometric structure of the Euclidean group SE(3) and its Lie algebra se(3) to seamlessly and accurately incorporate kinematic constraints, is also presented. In Section 3 we consider both analytically and numerically the body configurations and dynamics which emerge from the model equations. The case of a vanishing active moment is first explored, resulting in planar dynamics. The results of a linear stability analysis are shown to compare favorably with full numerical simulations, and associated eigenfunctions provide a baseline from which to explore a sequence of shape bifurcations in the fully nonlinear system. The fully three-dimensional dynamics are then probed, which reveal buckling behaviors analogous to those found in the planar setting, but which also involve a coupling between twisting and bending modes of deformation and stress. A linear stability analysis is revisited, which includes modifications to the predicted unstable wavenumbers and growth rates in the case with no active moment. We close with a discussion in Section 4 with directions for future study.

2. Active Kirchhoff rod model

The cell is assumed to have length L with uniform circular cross-section of diameter a. Aspect ratios a/L of swarmers, typically on the order of 10^{-2} to 5×10^{-2},[27,56] are sufficiently small that extensile and shear deformations are neglected.[57] Associated with each station of the filament in arclength s and time t is a matrix $\Phi(s,t) = \begin{pmatrix} Q & \mathbf{r} \\ 0 & 1 \end{pmatrix}$ representing the Euclidean transformation which maps an inertial frame $(\mathbf{e}_0, \mathbf{e}_1, \mathbf{e}_2)$ located at the origin onto the body's orthonormal material frame $(\mathbf{q}_0, \mathbf{q}_1, \mathbf{q}_2) = (Q\mathbf{e}_0, Q\mathbf{e}_1, Q\mathbf{e}_2)$ located at $\mathbf{r}$. Velocities and deformations may then be represented by the fields

$$\Psi_t = \Phi^{-1}\partial_t\Phi = \begin{pmatrix} \hat{\omega} & \mathbf{u} \\ 0 & 0 \end{pmatrix}, \qquad (1)$$

$$\Psi_s = \Phi^{-1}\partial_s\Phi = \begin{pmatrix} \hat{\Omega} & \mathbf{U} \\ 0 & 0 \end{pmatrix}, \tag{2}$$

where we have defined the antisymmetric operators $\hat{\omega} := \omega\times$ and $\hat{\Omega} := \mathbf{\Omega}\times$. The generalized velocity Ψ_t describes the body's local linear velocity, $\mathbf{u} = Q^{-1}\partial_t\mathbf{r}$, and local angular velocity, $\hat{\omega} = Q^{-1}\partial_t Q$, as measured in the material frame, and the field Ψ_s describes the body's local deformation in the form of the twist/curvature operator, $\hat{\Omega} = Q^{-1}\partial_s Q$, and the centerline tangent vector $\mathbf{U} = Q^{-1}\partial_s\mathbf{r}$. We choose to formulate dynamics of the body directly in terms of the fields $\left(\mathbf{u}, \hat{\omega}, \mathbf{U}, \hat{\Omega}\right)$, and write body configurations as path-ordered exponentials,[58]

$$\Phi(0,t) = \Phi(0,0)\mathrm{P}\exp\int_0^t \Psi_t(0,\xi)d\xi, \tag{3}$$

$$\Phi(s,t) = \Phi(0,t)\mathrm{P}\exp\int_0^s \Psi_s(\xi,t)d\xi. \tag{4}$$

The path-ordered exponential, or product integral, of a matrix-valued curve $X = X(\xi)$ is the limit of an ordered product of matrix exponentials,

$$\mathrm{P}\exp\int_a^b X(\xi)d\xi = \lim_{n\to\infty} e^{X(\xi_0)\Delta\xi}e^{X(\xi_1)\Delta\xi}\cdots e^{X(\xi_n)\Delta\xi}, \tag{5}$$

where $\Delta\xi = (b-a)/n$ and $\xi_k = a + k\Delta\xi$. Integrability of the system $\Phi^{-1}d\Phi = \Psi_s ds + \Psi_t dt$ requires Ψ_s and Ψ_t satisfy the Euclidean structure equations,[59]

$$\partial_s\omega - \partial_t\mathbf{\Omega} + \mathbf{\Omega}\times\omega = \mathbf{0}, \tag{6}$$

$$\partial_s\mathbf{u} - \partial_t\mathbf{U} + \mathbf{\Omega}\times\mathbf{u} - \omega\times\mathbf{U} = \mathbf{0}, \tag{7}$$

which are a generalization of the familiar compatibility relations for elastic rods.[48,57] A principal advantage of this approach is that it naturally leads to numerical schemes which circumvent violations of inextensibility, unshearability, and frame orthonormality, and do not require soft penalties or explicit parameterization of rotations by Euler angles or quaternions.[60–64]

Viscous stresses, $-\zeta\cdot\mathbf{u}$ and $-\zeta_r\omega_{||} = -(\mathbf{U}\cdot\omega)\mathbf{U}$, are related to the local body velocity through a local resistive force theory, where $\zeta = \zeta_{||}\mathbf{U}\mathbf{U}^T + \zeta_\perp(1 - \mathbf{U}\mathbf{U}^T)$ with longitudinal $\zeta_{||}$ and transverse $\zeta_\perp$ coefficients, and by a rotational drag coefficient ζ_r.[46,65] Driving the system away from equilibrium are active stresses arising from a distribution of flagella, modeled here as a continuum providing an effective tangential force density $f\mathbf{U}$ and proportional moment density $m\mathbf{U} := MLf\mathbf{U}$ (Fig. 1e). To account for the tendency of flagella to align with local flow, we consider f to evolve according to

$$\tau_f\partial_t f = (f^*/L)[1 - (f/f^*)^2]\mathbf{U}\cdot\mathbf{u} + D_f\partial_s^2 f, \tag{8}$$

with $\partial_s f(-L/2) = \partial_s f(L/2) = 0$. The force density tends toward a characteristic magnitude f^* with a relaxation time $\tau_f\zeta_{||}L/f^*$ depending on the dimensionless parameter τ_f, and D_f is a diffusion constant.

The internal energy of the body is given by

$$E = \int_{-L/2}^{L/2} \frac{1}{2}\mathbf{\Omega}\cdot\mathbf{B}\mathbf{\Omega} + \mathbf{\Lambda}\cdot\mathbf{U}ds \tag{9}$$

where $\mathbf{\Lambda}$ is a Lagrange multiplier which enforces inextensibility and unshearability,

$$\mathbf{q}_0 = Q\mathbf{U} \tag{10}$$

and $\mathbf{B} = B_{||}\mathbf{U}\mathbf{U}^T + B_\perp(1 - \mathbf{U}\mathbf{U}^T)$ penalizes twisting and bending with moduli $B_{||}$ and $B_\perp$, respectively.[57] Balancing structure preserving variations[53] of E with active and viscous work gives the Euler-Poincaré equations,

$$\partial_s\mathbf{\Lambda} + \mathbf{\Omega}\times\mathbf{\Lambda} = \zeta\cdot\mathbf{u} - f\mathbf{U}, \tag{11}$$

$$\partial_s(\mathbf{B}\mathbf{\Omega}) + \mathbf{\Omega}\times\mathbf{B}\mathbf{\Omega} + \mathbf{U}\times\Lambda = \zeta_r\omega_{||} - m\mathbf{U}, \tag{12}$$

which describe local force and moment balance (see Appendix B). The kinematic relations (3), (4), (6), (7), (10), the flagellar evolution law (8), and the balance eqn (11), (12) form a closed system describing dynamics of the body and its flagellar distribution.

Evolution equations for the twist $\mathbf{\Omega}_{||} = (\mathbf{U}\cdot\mathbf{\Omega})\mathbf{U}$, curvatures $\mathbf{\Omega}_\perp = (1 - \mathbf{U}\mathbf{U}^T)\mathbf{\Omega}$, and tension $\lambda = \mathbf{U}\cdot\mathbf{\Lambda}$ are obtained by first solving (10)–(12) and the transverse part of (7) for $\mathbf{\Lambda}_\perp = (1 - \mathbf{U}\mathbf{U}^T)\mathbf{\Lambda}$ and the velocities $(\omega, \mathbf{u})$:

$$\mathbf{\Lambda}_\perp = \mathbf{U}\times\partial_s(B_\perp\mathbf{\Omega}_\perp) + (B_{||} - B_\perp)(\mathbf{U}\cdot\mathbf{\Omega}_{||})\mathbf{\Omega}_\perp, \tag{13}$$

$$\mathbf{u} = \zeta^{-1}(\partial_s\mathbf{\Lambda} + \mathbf{\Omega}\times\mathbf{\Lambda} + f\mathbf{U}), \tag{14}$$

$$\omega = \frac{1}{\zeta_r}(\partial_s(B_{||}\mathbf{\Omega}_{||}) + m\mathbf{U}) + \mathbf{U}\times(\partial_s\mathbf{u} + \mathbf{\Omega}\times\mathbf{u}). \tag{15}$$

Eqn (13)–(15) are then substituted into eqn (6) and the longitudinal component of (7). The resulting shape evolution equations take the form

$$\partial_t\mathbf{\Omega}_{||} + \left[\frac{B_\perp - B_{||}}{\zeta_\perp}\kappa^2 - \frac{B_{||}}{\zeta_r}\right]\partial_s^2\mathbf{\Omega}_{||} = \mathbf{G}_{||}, \tag{16}$$

$$\partial_t\mathbf{\Omega}_\perp + \frac{B_\perp}{\zeta_\perp}\partial_s^4\mathbf{\Omega}_\perp = \mathbf{G}_\perp, \tag{17}$$

$$\partial_s^2\lambda - \frac{\zeta_{||}}{\zeta_\perp}\kappa^2\lambda + \frac{B_\perp}{2}\partial_s^2\kappa^2 + \partial_s f$$
$$+ \frac{\zeta_{||}B_\perp}{\zeta_s}(\mathbf{\Omega}_s\cdot\partial_s^2\mathbf{\Omega}_\perp - \kappa^2|\mathbf{\Omega}_{||}|^2 - 2\mathbf{\Omega}_{||}\cdot[\mathbf{\Omega}_\perp\times\partial_s\mathbf{\Omega}_\perp])$$
$$+ \frac{\zeta_{||}B_{||}}{\zeta_\perp}(\kappa^2|\mathbf{\Omega}_{||}|^2 + \mathbf{\Omega}_{||}\cdot[\mathbf{\Omega}_\perp\times\partial_s\mathbf{\Omega}_\perp]) = 0, \tag{18}$$

where we have defined $\kappa^2 = |\mathbf{\Omega}_\perp|^2$, and the vector-valued functions $\mathbf{G}_{||}$ and $\mathbf{G}_\perp$ depend nonlinearly on spatial derivatives of $\mathbf{\Omega}$, λ, and f. Natural boundary conditions require that $\Omega_{||}$, $\mathbf{\Omega}_\perp$, $\partial_s\mathbf{\Omega}_\perp$, and λ all vanish at both ends of the body.

Upon scaling by the length L, force density f^*, and stiffness $B_\perp$, the system is found to depend on six dimensionless groups: a relative bending modulus $\beta_\perp = B_\perp/(f^*L^3)$, twist modulus $\beta_{||} = B_{||}/(f^*L^3)$, translational drag ratio $\eta = \zeta_\perp/\zeta_{||}$,

rotational drag $\eta_r = \zeta_r/(\zeta_{||}L^2)$, dimensionless active moment M, and a dimensionless diffusion constant $D = \zeta_{||}D_f/(f^*L)$. Henceforth all variables are understood to be dimensionless.

To estimate the scale of the active moment, M, we note that a helical flagellum with pitch $P \approx 2$ μm, circumference $C \approx 1.5$ μm, length $\ell = 10$ μm, and diameter $d \approx 20$ nm, upon rotation with speed ω generates a force on an affixed body $F_\nu \approx 2\mu C^2 \ell \omega/Pc$, where μ is the viscosity of water and $c = \ln(\ell^2/d^2) - 1$.[66] Due to its chirality it also generates a torque $L_\nu \approx 2\mu C^2 \ell \omega/\pi^2 c$. Using a body length $L \approx 10^{-5}$–10^{-4} m gives a range of biologically relevant active moments $M = L_\nu/LF_\nu \approx 10^{-3}$–$10^{-2}$.

Eqn (8), (16)–(18) are discretized in space uniformly using second-order accurate central difference approximations, and advanced in time using a second-order implicit backward-differentiation scheme with a hybrid nonlinear solver applied at each timestep. Eqn (3) and (4) are solved using explicit second-order accurate Magnus integrators[67,68] (see Appendix A.2). Other approaches to this stiff numerical problem with different treatments of the hydrodynamics have recently been developed.[69–78] The parameters $(\eta, D, \tau_f) = (2, 10^{-3}, 10^{-2})$, timestep size $\Delta t = 10^{-3}$, and spatial gridspacing $\Delta s = 1/64$ are fixed for the duration unless otherwise stated.

3. Body configurations and dynamics

3.1 No active moment: planar dynamics

In the case of no active moment, $M = 0$, the body configuration is fully characterized by a single rotational strain, the (signed) centerline curvature $\kappa = \pm|\boldsymbol{\Omega}_\perp|$. Restricting the shape evolution equations to two dimensions, the curvature, active force, and tension satisfy

$$\partial_t \kappa = -\frac{\beta_\perp}{\eta}\partial_s^4 \kappa + \frac{1}{\eta}\partial_s^2(\kappa\lambda) + \partial_s(\kappa[\partial_s\lambda + f]) + \frac{\beta_\perp}{3}\partial_s^2(\kappa^3), \quad (19)$$

$$\partial_t f = D\partial_s^2 f + (1 - f^2)(\beta_\perp \kappa\partial_s\kappa + \partial_s\lambda + f), \quad (20)$$

$$\partial_s^2\lambda - \frac{\kappa^2}{\eta}\lambda = -\partial_s f - \frac{\beta_\perp}{2}\partial_s^2(\kappa^2) - \frac{\beta_\perp}{\eta}\kappa\partial_s^2\kappa. \quad (21)$$

To begin we consider shapes which are symmetric about the body midpoint $s = 0$ (and active forces which are odd). To describe the geometry it is convenient to use the eigenfunctions of ∂_s^4 satisfying force- and moment-free boundary conditions[79] (the first three of which are shown in Fig. 2c as dashed red curves). The curvature is decomposed as a sum

$\kappa(s,t) = \sum_{k=0}^{\infty} a_k(t)\phi_k(s)$. Fig. 1g shows a phase portrait for the dynamics of the first two even biharmonic modes, (a_0, a_2), for a range of bending stiffness $\beta_\perp$ with $M = 0$. Values are plotted against $\beta_\perp^{-1/3}$, which is proportional to the body length L.

Phases in Fig. 1g are identified by examining the long time behaviour of filaments initialized with a compressive active force density $f(s,0) = -\tanh(10s)$. For $\beta_\perp > 9.1 \times 10^{-3}$, the stiff filament relaxes to a straight configuration, with the active stress eventually decaying due to diffusion via eqn (8). At approximately $\beta_\perp = 9 \times 10^{-3}$ there is a bifurcation to steady state U-shaped swimmers with a nonzero a_0 which dominates
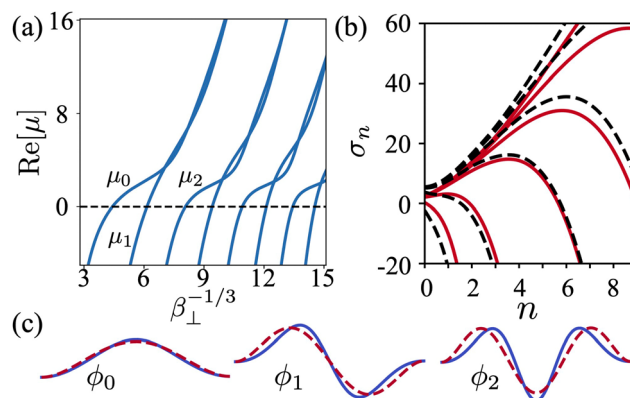

Fig. 2 (a) Dominant eigenvalues μ_n of the linearized curvature dynamics with no active moment and a piecewise constant force density show the emergence of multiple unstable modes at critical bending stiffnesses; the first at $\beta_\perp \approx 1.0 \times 10^{-2}$, or $\beta_\perp^{-1/3} \approx 4.6$. (b) Growth rates of biharmonic eigenfunctions, $\phi_n(s)$, in the fully nonlinear system with $M = 0$ (solid lines) and $M = 0.01$ (dashed). (c) First three unstable modes of the linearized system (solid), and biharmonic eigenfunctions (dashed).

all other modes. Further decreases in stiffness lead to curvature oscillations (this cross-section of the phase diagram is shown in Fig. 1h) and excitation of progressively higher modes. At approximately $\beta_\perp = 6.8 \times 10^{-5}$, another bifurcation is observed to unsteady, periodic flapping dynamics which involve even larger excursions in the phase plane (Fig. 1i), and periodic changes in the swimming direction.

Susceptibility to buckling can be understood by exploring the stability of a nearly straight body to generic (planar) perturbations. Upon defining the mean active force density $\bar{f} := \int_{-1/2}^{1/2} f \, ds$, we find to first order in κ (assumed small) that

$$\lambda = -\int_{-1/2}^{s}(f - \bar{f})\mathrm{d}s, \quad (22)$$

$$\partial_t \kappa = -\frac{\beta_\perp}{\eta}\partial_s^4\kappa + \frac{1}{\eta}\partial_s^2(\lambda\kappa) + \bar{f}\partial_s\kappa. \quad (23)$$

Assuming a symmetric compressive force, $\bar{f} = 0$, this yields an eigenvalue problem,

$$\mathscr{L}[\kappa] = -\frac{\beta_\perp}{\eta}\partial_s^2\left(\partial_s^2\kappa - \frac{1}{\beta_\perp}\lambda\kappa\right),$$

$$\mathscr{L}[\kappa] = \mu\kappa. \quad (24)$$

Fig. 2a shows the (real part) of dominant eigenvalues μ_n of eqn (26) for a range of stiffness $\beta_\perp$. The unstable modes of the linear system are illustrated in Fig. 2c by solid blue curves, along with the biharmonic eigenfunctions for comparison. Growth rates $\sigma_n = \partial_t a_n(t)|_{t=0}/a_n(0)$, computed using the fully nonlinear system, eqn (21)–(23), with $a_n(0) = 10^{-3}$ are shown in Fig. 2b.

To identify the critical values of $\beta_\perp$ where different spatial modes become unstable, we set $\mu = 0$ and seek solutions to $\mathcal{L}[\kappa] = 0$. For a piecewise constant force density, $f(s) = 1 - 2H(s)$, where $H(s)$ the Heaviside step function, critical values for even

modes using eqn (26) are given by the solutions of

$$\text{Bi}'(\xi)\int_0^\xi \text{Ai}(x)\mathrm{d}x - \text{Ai}'(\xi)\int_0^\xi \text{Bi}(x)\mathrm{d}x = 0, \qquad (25)$$

where Ai and Bi are the Airy functions of the first and second kind, and $\xi = -\beta_\perp^{-1/3}/2$ (see Appendix C). For odd modes they are given by solutions of

$$-\xi\text{Bi}(\xi)\int_0^\xi \text{Ai}(x)\mathrm{d}x + \xi\text{Ai}(\xi)\int_0^\xi \text{Bi}(x)\mathrm{d}x$$
$$+ \text{Bi}'(0)\text{Ai}(\xi) - \text{Ai}'(0)\text{Bi}(\xi) - 1/\pi = 0. \qquad (26)$$

When compared to the first ten critical stiffnesses in the fully nonlinear dynamics with regularized active force density, predictions of eqn (27) and (28) were found to differ by 0.5–15%. The first bending stiffness below which the filament becomes unstable from the full system is $\beta_\perp = 1.0 \times 10^{-2}$, whereas the linearized dynamics predict $\beta_\perp = 1.1 \times 10^{-2}$.

3.2 Inclusion of an active moment: three-dimensional dynamics

We turn now to the fully three-dimensional system, including the active moment contribution due to flagellar chirality ($M \neq 0$). Numerous dynamical regimes appear as the result of rotational forcing (see Movie M7, ESI†), with transitions between newly emergent phases brought about by variations in any one of the twisting stiffness, $\beta_{||}$, bending stiffness, $\beta_\perp$, or active moment, M.

As with the 2D system, we seek a reduced order phase space in which to study these bifurcations. To this end, we consider systems initialized with the twist Ω_0 and curvature Ω_2 even about the midpoint, and the curvature Ω_1 odd. This is equivalent to the system possessing a π-rotational symmetry, and,

provided the initial active stress distributions are odd functions of s about the midpoint, this symmetry is conserved. Taking advantage of their conserved parity, the twist and curvatures may be decomposed into sums of harmonic γ_{2k} and biharmonic $\{\phi_{2k}, \phi_{2k+1}\}$ functions satisfying appropriate parity and boundary and conditions:

$$\Omega_0(s, t) = \sum_k b_{2k}(t)\gamma_{2k}(s), \qquad (27)$$

$$\Omega_1(s, t) = \sum_k a_{2k+1}^{(1)}(t)\phi_{2k+1}(s), \qquad (28)$$

$$\Omega_2(s, t) = \sum_k a_{2k}^{(2)}(t)\phi_{2k}(s). \qquad (29)$$

Fig. 3a–d shows characteristic shapes of four observed phases (top), as well as corresponding phase space trajectories of $(b_0, a_1, a_0) := (b_0, a_1^{(1)}, a_0^{(2)})$ appearing in the decomposition of twist/curvatures for a range of initial conditions (bottom). For $\beta_{||} < 2.5 \times 10^{-4}$, $\beta_\perp > 7.5 \times 10^{-4}$, and $M > 1.4 \times 10^{-2}$ the body adopts a straight configuration. A bifurcation to a twisted-U shape appears upon increasing $\beta_{||}$, decreasing $\beta_\perp$, or decreasing M (Fig. 3a). With $M < 1.8 \times 10^{-2}$, the twisted-U phase persists as $\beta_\perp$ is decreased until approximately $\beta_\perp = 2 \times 10^{-4}$, at which point the system develops periodic oscillations (Fig. 3b, see Movie M5, ESI†). Again with $M < 1.8 \times 10^{-2}$, new S-shaped equilibria emerge for $\beta_\perp < 1 \times 10^{-4}$ (Fig. 3c). A fourth phase appears for $M > 1.8 \times 10^{-2}$ and $\beta_\perp < 2.5 \times 10^{-4}$ with twist-curvature oscillations accompanied by periodic changes in swimming direction (Fig. 3d, see Movie M6, ESI†).

Transitions between phases can lead to wide variations in swimming trajectories, and in the swimming speed, defined as the magnitude of the average velocity of the body's midpoint in
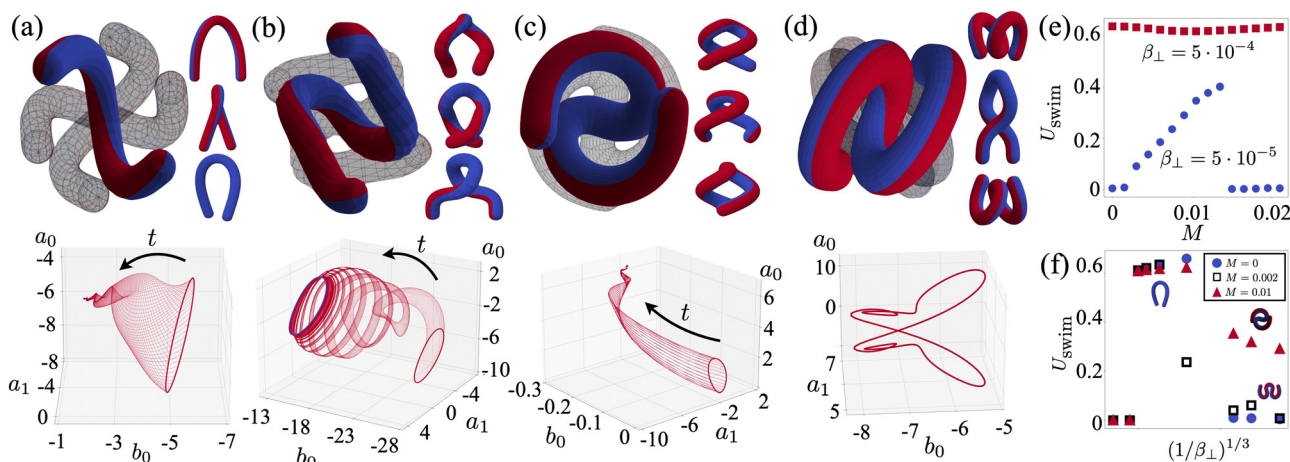
Fig. 3 (a–d) New attractors emerge upon the addition of an active moment (with body symmetry assumed). Top-snapshots of body configurations over a half-period, bottom – trajectories of the first two bending (a_0, a_1) and the first twisting (b_0) mode coefficients suggests convergence to a fixed shape. (a) ($\beta_{||}$, $\beta_\perp$, M) = (1×10^{-4}, 2.5×10^{-4}, 6×10^{-3}): (a) U-shaped swimmer with a twist. (b) ($\beta_{||}$, $\beta_\perp$, M) = (1×10^{-5}, 8×10^{-5}, 1.35×10^{-2}): reduced stiffness and increased active moment introduces a limit cycle corresponding to waving while twisting (see Movie M5, ESI†). (c) ($\beta_{||}$, $\beta_\perp$, M) = (1×10^{-3}, 5.45×10^{-5}, 1×10^{-2}): convergence to a new twisted-S shape. (d) ($\beta_{||}$, $\beta_\perp$, M) = (1×10^{-3}, 1.25×10^{-4}, 2×10^{-2}): periodic flapping appears with further increases in M (see Movie M6, ESI†). (e) Swimming speed across a range of active moments for $\beta_{||} = 2.5 \times 10^{-4}$, for a stiffer ($\beta_\perp = 5 \times 10^{-4}$, squares) and softer ($\beta_\perp = 5 \times 10^{-5}$, circles) body. (f) Swimming speed across a range of bending stiffness for $\beta_{||} = 2.5 \times 10^{-4}$ and active moments $M = 0$ (circles), $M = 0.002$ (squares), and $M = 0.01$ (triangles).

the lab frame, $U_{\text{swim}}(T) = \left| \int_0^T Q(0, t)\mathbf{u}(0, t)dt \right| / T$. The complicated relationship between bend and twist is further illustrated by the nonmonotonic, and discontinuous, changes in swimming speed that arise due to variations in bending stiffness $\beta_\perp$ and active moment M. Fig. 3e shows the swimming speed as a function of the active moment for two different bending stiffnesses. For the stiffer body the active moment induces waving (from Fig. 3a to b, see Movie M5, ESI†) but the swimming speed remains roughly unchanged. For the softer body, however, which at $M = 0$ is in the dramatic flapping-W state in two dimensions (Fig. 1i), the introduction of the active moment can stabilize the shape in three dimensions and result in a ballistic trajectory (Fig. 3c). Further increases in M, however, then trigger another phase transition to the three-dimensional flapping dynamics of Fig. 3d (see Movie M6, ESI†), resulting in average speeds (but not instantaneous speeds) tending to zero. A different view is offered by Fig. 3f, which shows the swimming speed across a range of bending stiffnesses for three different active moments. A sufficiently large active moment can delay the onset of flapping dynamics, and thereby stabilize swimming trajectories over a larger range of stiffnesses.

At the lower bending stiffness typical of swarmer cells, rotational forcing introduces a dynamical twist-bend instability. As shown in Fig. 2b as dashed lines for $M = 0.01$, the presence of an active moment can decrease the force required to excite higher unstable modes. As described in relation to Fig. 3e above, this allows the system to access new energetically favorable out-of-plane equilibria similar to the 'locked curvature' configurations observed in model cilia.[38,43]

Though not explored in detail here, both of the low stiffness configurations shown in Fig. 3c and d are generically unstable with respect to asymmetric perturbations, which lead to non-periodic dynamics and trajectories which depend sensitively upon the bending stiffness (see Movie M8, ESI†). The self-contact evident in Fig. 1d, and self intersections observed at low bending stiffness in the model, suggest that steric interactions or nonlocal hydrodynamic effects are important for stabilizing body configurations of longer swarmer cells. Confinement by neighboring cells in bacterial swarms may play a similar role.

4. Discussion

We have shown that numerous behaviors of individual swimming *P. mirabilis* swarmer cells are qualitatively captured by an active Kirchhoff rod model. The relative bending stiffness $\beta_\perp = B_\perp / f^* L^3$, relating the flagellar stress to the cell's material and geometric properties, is seen to play an outsized role. Our analysis reveals a minimal value, approximately $\beta_\perp = 1.01 \times 10^{-2}$, required of a cell below which its motility is severely hampered by self-buckling. For *P. mirabilis* swarmer cells, this corresponds to a critical bending stiffness of $B_\perp = 2.6 \times 10^{-23}$ N m² (see Appendix C.1), approximately one order of magnitude lower than the experimentally determined stiffness of typical cells.[56] We propose that this offers some evidence that cells may develop and maintain mechanical properties to prevent

excessive buckling during motility. That the difference is not tighter may speak either to the approximations made in modeling the highly complex surface array of flagella, and/or related to the larger stresses that the organisms may experience inside of a swarm. This observation may offer insight relevant to the evolutionary development of motility, bacterial adaptation and survival, and potential mechanically-motivated medical interventions. Bifurcations in body shape produce significant changes in swimming trajectories, as we have begun to explore, but are also expected to affect the ways in which such bodies interact with one another. This likely has substantial consequences for the collective motion of bacterial swarms. We have only begun to scratch the surface of the high dimensional parameter space available to a generic active Kirchhoff rod. Characterization of critical parameter values which trigger bifurcations may provide novel experimental methods for quantifying mechanical properties of active, flexible bodies. Such methods may require a more detailed treatment of the hugely complex, flagellated surface, or a more elastic energy than we have assumed here. Our model is readily generalizable to include these additional complexities using (46) and (57), which do not assume a particular form for the elastic energy, activity, or viscous stress.

Conflicts of interest

There are no conflicts to declare.

Appendix

A Kinematics

A.1 Structure equations

We write se(3) to denote the Lie algebra of SE(3), the special Euclidean group in three dimensions. Deformation and velocity fields (Ψ_s, Ψ_t) are components of an se(3)-valued one-form,

$$\Psi = \Psi_s ds + \Psi_t dt = \Phi^{-1} d\Phi, \qquad (30)$$

where $d\Phi = \partial_s \Phi ds + \partial_t \Phi dt$ is the exterior derivative of Φ, and (ds, dt) are one-forms dual to the coordinate basis (∂_s, ∂_t). Repeated application of the exterior derivative gives

$$0 = d^2\Phi = \Phi d\Psi + d\Phi \wedge \Psi, \qquad (31)$$

where $\wedge$ is the wedge product for matrix-valued differential forms.[59] Multiplying by Φ^{-1} and using $\Psi = \Phi^{-1} d\Phi$ results in the Maurer–Cartan equation,

$$d\Psi + \Psi \wedge \Psi = 0. \qquad (32)$$

This gives the commutation relation,

$$(d\Psi + \Psi \wedge \Psi)(\partial_s, \partial_t) = \partial_s \Psi_t - \partial_t \Psi_s + [\Psi_s, \Psi_t] = 0, \quad (33)$$

where $[\Psi_s, \Psi_t] := \Psi_s \Psi_t - \Psi_t \Psi_s$ is the matrix commutator. Expressing (35) in terms of $\hat{\Omega}, \mathbf{U}, \hat{\omega}$ and $\mathbf{u}$, and using the fact that

Soft Matter

Paper

$\widehat{\mathbf{a} \times \mathbf{b}} = [\hat{\mathbf{a}}, \hat{\mathbf{b}}]$, for any $\mathbf{a}, \mathbf{b} \in \mathbb{R}^3$, gives eqn (6) and (7) found in the main text.

A.2 Shape and spatial orientation

Eqn (3) is equivalent to

$$\Phi(0, t + \xi) = \Phi(0, t) \mathrm{P} \exp \int_0^\xi Z(\xi') \mathrm{d}\xi', \qquad (34)$$

with $Z(\xi) := \Psi_t(0, t + \xi)$. The ordered exponential in (34) can be expressed as $P \exp \int_0^\xi Z(\xi') \mathrm{d}\xi' = \mathrm{e}^{X(\xi)}$, where X is an se(3)-valued field related to Z by the Magnus expansion

$$X(\xi) = \int_0^\xi Z(\xi) \mathrm{d}\xi - \frac{1}{2} \int_0^\xi \int_0^{\xi'} [Z(\xi'')Z(\xi')] \mathrm{d}\xi'' \mathrm{d}\xi' + \dots \quad (35)$$

and writing

$$X(\xi) = \xi \frac{Z(\xi) + Z(0)}{2} + O(\xi^3), \qquad (36)$$

we have

$$\mathbf{\Phi}(0, t + \Delta t) = \mathbf{\Phi}(0, t) \exp\left(\Delta t \frac{\mathbf{\Psi}_t(0, t + \Delta t) + \mathbf{\Psi}_t(0, t)}{2} \right) + O(\Delta t^3). \qquad (37)$$

By a similar argument, we find

$$\mathbf{\Phi}(s + \Delta s, t) = \mathbf{\Phi}(s, t) \exp\left(\Delta s \frac{\mathbf{\Psi}_s(s + \Delta s, t) + \mathbf{\Psi}_s(s, t)}{2} \right) + O(\Delta s^3). \qquad (38)$$

Matrix exponentials in (37) and (38) are computed using the closed form expression for the exponential map on SE(3). Given vectors $\boldsymbol{\alpha}$ and $\mathbf{b}$, defining the antisymmetric operator $\hat{\alpha} := \boldsymbol{\alpha} \times$ results in the relation

$$\exp\begin{pmatrix} \hat{\alpha} & \mathbf{b} \\ 0 & 0 \end{pmatrix} = \begin{pmatrix} e^{\hat{\alpha}} & V\mathbf{b} \\ 0 & 1 \end{pmatrix}, \qquad (39)$$

where $\quad \mathrm{e}^{\hat{\alpha}} = \mathrm{I} + \dfrac{\sin \alpha}{\alpha} \hat{\alpha} + \dfrac{1 - \cos \alpha}{\alpha^2} \hat{\alpha}^2, \qquad V = \mathrm{I} + \dfrac{1 - \cos \alpha}{\alpha^2} \hat{\alpha} + \dfrac{\alpha - \sin \alpha}{\alpha^3} \hat{\alpha}^2$, and $\alpha = |\boldsymbol{\alpha}|$.

B. Derivation of Euler–Poincaré equations

The Euler–Poincaré equations, which govern local force and moment balance along the body, are obtained using a constrained variational principal. The variation $\delta \mathbf{\Phi} := \partial_\xi \tilde{\mathbf{\Phi}}(\xi)|_{\xi=0}$ is given by the derivative of a field, $\tilde{\mathbf{\Phi}} = \tilde{\mathbf{\Phi}}(s, t, \xi)$, which satisfies $\tilde{\mathbf{\Phi}}(s, t, 0) = \mathbf{\Phi}(s, t)$.[80] The associated 1-form $\tilde{\mathbf{\Psi}} = \tilde{\mathbf{\Psi}}_s \mathrm{d}s + \tilde{\mathbf{\Psi}}_t \mathrm{d}t + \tilde{\mathbf{\Psi}}_\xi \mathrm{d}\xi := \tilde{\mathbf{\Phi}}^{-1} \mathrm{d}\tilde{\mathbf{\Phi}}$ now includes a ξ-component which acts as the generator of variations $\delta \mathbf{\Phi} = \mathbf{\Phi} \tilde{\mathbf{\Psi}}_\xi|_{\xi=0} =: \mathbf{\Phi} \mathbf{\Psi}_\xi$. It follows directly from the definitions of $(\mathbf{\Psi}, \tilde{\mathbf{\Psi}}, \tilde{\mathbf{\Phi}})$ that $\tilde{\mathbf{\Psi}}_s(s, t, 0) = \mathbf{\Psi}_s(s, t)$, so, the variation $\delta \mathbf{\Psi}_s(s, t) = \partial_\xi \tilde{\mathbf{\Psi}}_s(s, t, \xi)|_{\xi=0}$ is constrained by the Maurer–Cartan equation,

$$(\mathrm{d}\tilde{\mathbf{\Psi}} + \tilde{\mathbf{\Psi}} \wedge \tilde{\mathbf{\Psi}})(\partial_s, \partial_\xi)|_{\xi=0} = \partial_s \mathbf{\Psi}_\xi - \delta \mathbf{\Psi}_s + [\mathbf{\Psi}_s, \mathbf{\Psi}_\xi] = 0. \qquad (40)$$

In terms of angular and linear components of $\mathbf{\Psi}_\xi = \begin{pmatrix} \hat{\omega}_\xi & \mathbf{u}_\xi \\ 0 & 0 \end{pmatrix}$, eqn (40) reads

$$\delta \mathbf{\Omega} - \partial_s \boldsymbol{\omega}_\xi + \boldsymbol{\omega}_\xi \times \mathbf{\Omega} = \mathbf{0} \qquad (41)$$

$$\delta \mathbf{U} - \partial_s \mathbf{u}_\xi + \boldsymbol{\omega}_\xi \times \mathbf{U} - \mathbf{\Omega} \times \mathbf{u}_\xi = \mathbf{0}. \qquad (42)$$

We define the inner product for se(3)-valued matrices $X = \begin{pmatrix} \hat{\omega}_X & \mathbf{u}_X \\ 0 & 0 \end{pmatrix}$ and $Y = \begin{pmatrix} \hat{\omega}_Y & \mathbf{u}_Y \\ 0 & 0 \end{pmatrix}$ by $\langle X, Y \rangle := \boldsymbol{\omega}_X \cdot \boldsymbol{\omega}_Y + \mathbf{u}_X \cdot \mathbf{u}_Y$ and the coadjoint operator, $\mathrm{ad}_{\psi_s}^*$, by $\langle \mathrm{ad}_{\psi_s}^* X, Y \rangle := \langle X, [\psi_s, Y] \rangle$. In terms of angular and linear components, we find

$$\mathrm{ad}_{\psi_s}^* X = -\begin{pmatrix} \widehat{\mathbf{\Omega} \times \boldsymbol{\omega}_X} + \widehat{\mathbf{U} \times \mathbf{u}_X} & \mathbf{\Omega} \times \mathbf{u}_X \\ 0 & 0 \end{pmatrix}. \qquad (43)$$

With an internal energy density $\mathscr{E} = \mathscr{E}(Q, \mathbf{r}, \mathbf{\Omega}, \mathbf{U})$, the variation of $E = \int_{-L/2}^{L/2} \mathscr{E} \, \mathrm{d}s$ generated by $\mathbf{\Psi}_\xi$ is

$$\delta E = \int_{-L/2}^{L/2} \left\langle -\partial_s \frac{\delta \mathscr{E}}{\delta \mathbf{\Psi}_s} + \mathrm{ad}_{\mathbf{\Psi}_s}^* \frac{\delta \mathscr{E}}{\delta \mathbf{\Psi}_s} + \Phi^{-1} \frac{\delta \mathscr{E}}{\delta \Phi}, \mathbf{\Psi}_\xi \right\rangle \mathrm{d}s + \left\langle \frac{\partial \mathscr{E}}{\partial \mathbf{\Psi}_s}, \mathbf{\Psi}_\xi \right\rangle \Big|_{-L/2}^{L/2}. \qquad (44)$$

Balancing δE with the virtual work, $\mathcal{W} = \int_{-L/2}^{L/2} \langle N, \psi_\xi \rangle \mathrm{d}s$, done by nonconservative stresses, $N = \begin{pmatrix} \hat{\mathbf{M}} & \mathbf{F} \\ 0 & 0 \end{pmatrix}$, with $\hat{M} := \mathbf{M} \times$ for vector $\mathbf{M}$, results in the Euler–Poincaré equations,

$$-\partial_s \frac{\delta \mathscr{E}}{\delta \mathbf{\Psi}_s} + \mathrm{ad}_{\mathbf{\Psi}_s}^* \frac{\delta \mathscr{E}}{\delta \mathbf{\Psi}_s} + \Phi^{-1} \frac{\delta \mathscr{E}}{\delta \Phi} = N. \qquad (45)$$

Separating (45) into its linear and angular parts gives

$$-(\partial_s + \mathbf{\Omega} \times) \nabla_\Omega \mathcal{E} - \mathbf{U} \times \nabla_\mathbf{U} \mathcal{E} + Q^{\mathrm{T}}(\mathbf{q}_i \times \nabla_{\mathbf{q}_i} \mathcal{E}) = \mathbf{M}, \quad (46)$$

$$-(\partial_s + \mathbf{\Omega} \times) \nabla_\mathbf{U} \mathscr{E} + Q^T \nabla_\mathbf{r} \mathscr{E} = \mathbf{F}, \qquad (47)$$

where the repeated index implies summation. Natural boundary conditions are given by

$$(\nabla_\Omega \mathscr{E}, \nabla_\mathbf{U} \mathscr{E})|_{s=\pm L/2} = (0, 0). \qquad (48)$$

C. Critical $\beta_\perp$ values for $f(s) = 1 - 2H(s)$

Critical values of $\beta := \beta_\perp$ at which different spatial modes become unstable are associated with the emergence of nontrivial solutions to (24) with $\mu = 0$. With the piecewise constant active force, $f(s) = 1 - 2H(s)$, with $H(s)$ the Heaviside step function, the tension is given by

$$\lambda(s) = 2sH(s) - (s + 1/2) = \begin{cases} -(s + 1/2) & -1/2 < s < 0, \\ s - 1/2 & 0 < s < 1/2. \end{cases} \qquad (49)$$

After integrating (24) twice we find

$$\partial_s^2 \kappa - \frac{1}{\beta}\lambda\kappa = c^- s + c^+, \tag{50}$$

for constants c^- and c^+. When $\lambda(s) = \lambda(-s)$, eqn (24) is invariant under $\kappa(s) \mapsto \kappa(-s)$, so, we may assume eigenfunctions have definite parity. When $\kappa(-s) = \kappa(s)$, we find $c^- = 0$, and when $\kappa(-s) = -\kappa(s)$ we find $c^+ = 0$. Restricting to the half interval, $-1/2 < s < 0$ and introducing $\xi = \beta^{-1/3}\lambda = -(1 + 2s)/(2\beta^{1/3})$, we find κ satisfies a nonhomogeneous Airy equation on $-1/(2\beta^{1/3}) < \xi < 0$,

$$\partial_\xi^2 \kappa - \xi\kappa = a\xi + b, \tag{51}$$

$$\kappa|_{\xi=0}, \ \partial_\xi\kappa|_{\xi=0} = 0, \tag{52}$$

where $(a, b) = (-\beta^{1/3}c^-, c^+ - c^-/2)$. The solution to (51) and (52) is given by

$$\begin{aligned}\kappa(\xi) &= -\pi\mathrm{Ai}(\xi)\int_0^\xi (ax + b)\mathrm{Bi}(x)\mathrm{d}x + \pi\mathrm{Bi}(\xi)\int_0^\xi (ax + b)\mathrm{Ai}(x)\mathrm{d}x \\ &= \pi a[\mathrm{Bi}'(0)\mathrm{Ai}(\xi) - \mathrm{Ai}'(0)\mathrm{Bi}(\xi) - 1/\pi] \\ &\quad + \pi b\left[\mathrm{Bi}(\xi)\int_0^\xi \mathrm{Ai}(x)\mathrm{d}x - \mathrm{Ai}(\xi)\int_0^\xi \mathrm{Bi}(x)\mathrm{d}x\right],\end{aligned}$$

where

$$\mathrm{Ai}(\xi) = \frac{1}{\pi}\int_0^\infty \cos\left(\frac{x^3}{3} + \xi x\right)\mathrm{d}x, \tag{53}$$

$$\mathrm{Bi}(\xi) = \frac{1}{\pi}\int_0^\infty \sin\left(\frac{x^3}{3} + \xi x\right) + e^{-x^3/3 + \xi x}\mathrm{d}x \tag{54}$$

are Airy functions, and primes denote derivatives. Writing $\xi^* = -\beta^{-1/3}/2$, parity conditions require $(a, \partial_\xi\kappa|_{\xi^*}) = (0,0)$, giving

$$\kappa(\xi) = \mathrm{Bi}(\xi)\int_0^\xi \mathrm{Ai}(x)\mathrm{d}x - \mathrm{Ai}(\xi)\int_0^\xi \mathrm{Bi}(x)\mathrm{d}x, \tag{55}$$

$$\mathrm{Bi}'(\xi^*)\int_0^{\xi^*} \mathrm{Ai}(x)\mathrm{d}x - \mathrm{Ai}'(\xi^*)\int_0^{\xi^*} \mathrm{Bi}(x)\mathrm{d}x = 0, \tag{56}$$

and $(b/a, \kappa|_{\xi^*}) = (-\xi^*, 0)$, giving

$$\begin{aligned}\kappa(\xi) &= \mathrm{Bi}'(0)\mathrm{Ai}(\xi) - \mathrm{Ai}'(0)\mathrm{Bi}(\xi) - 1/\pi \\ &\quad - \xi^*\left(\mathrm{Bi}(\xi)\int_0^\xi \mathrm{Ai}(x)\mathrm{d}x - \mathrm{Ai}(\xi)\int_0^\xi \mathrm{Bi}(x)\mathrm{d}x\right),\end{aligned} \tag{57}$$

$$\begin{aligned}&\mathrm{Bi}'(0)\mathrm{Ai}(\xi^*) - \mathrm{Ai}'(0)\mathrm{Bi}(\xi^*) - 1/\pi \\ &- \xi^*\left(\mathrm{Bi}(\xi^*)\int_0^{\xi^*} \mathrm{Ai}(x)\mathrm{d}x - \mathrm{Ai}(\xi^*)\int_0^{\xi^*} \mathrm{Bi}(x)\mathrm{d}x\right) = 0,\end{aligned} \tag{58}$$

for even and odd eigenfunctions, respectively.

C.1 Estimate of critical dimensional bending stiffness

Swarmers with lengths in the range $L = 10$–100 μm were found to swim with an average velocity $u^* = 13$ μm s^{-1} when placed in a motility buffer with viscosity $\mu = 0.001$ Pa s.[24] Using the critical dimensionless bending stiffness $\beta_\perp^* = 0.0101$, a body

diameter of $a = 1$ μm, a longitudinal drag coefficient $\zeta_\parallel = 2\pi\mu/\ln(L/a)$, and characteristic force density $f^* = \zeta_\parallel u^*$, we predict the critical dimensional bending stiffness for swarmer cells to be in the range $B_\perp \approx 3.6 \times 10^{-25}$–$1.8 \times 10^{-22}$ N m^2. Experimental measurements have suggested an average swarmer cell bending stiffness of 5.5×10^{-22} N m^2.[56] Taking a characteristic body length of $L = 50$ μm results in a critical value of $B_\perp \approx 2.6 \times 10^{-23}$ N m^2.

Acknowledgements

Notes and references

1 R. Vogel and H. Stark, *Eur. Phys. J. E: Soft Matter Biol. Phys.*, 2012, **35**, 15.
2 M. K. Jawed, N. K. Khouri, F. Da, E. Grinspun and P. M. Reis, *Phys. Rev. Lett.*, 2015, **115**, 168101.
3 F. T. M. Nguyen and M. D. Graham, *Phys. Rev. E*, 2018, **98**, 042419.
4 Z. Zou, W. Lough and S. Spagnolie, *Phys. Rev. Fluids*, 2021, **6**, 103102.
5 K. D. Young, *Microbiol. Mol. Biol. Rev.*, 2006, **70**, 660.
6 W. F. Marshall, K. D. Young, M. Swaffer, E. Wood, P. Nurse, A. Kimura, J. Frankel, J. Wallingford, V. Walbot and X. Qu, *et al.*, *BMC Biol.*, 2012, **10**, 1.
7 L. Willis and K. C. Huang, *Nat. Rev. Microbiol.*, 2017, **15**, 606.
8 F. Si, G. Le Treut, J. T. Sauls, S. Vadia, P. A. Levin and S. Jun, *Curr. Biol.*, 2019, **29**, 1760.
9 J. E. Avron, O. Gat and O. Kenneth, *Phys. Rev. Lett.*, 2004, **93**, 186001.
10 S. E. Spagnolie and E. Lauga, *Phys. Fluids*, 2010, **22**, 031901.
11 R. Schuech, T. Hoehfurtner, D. J. Smith and S. Humphries, *Proc. Natl. Acad. Sci. U. S. A.*, 2019, **116**, 14440.
12 H. H. Tuson, G. K. Auer, L. D. Renner, M. Hasebe, C. Tropini, M. Salick, W. C. Crone, A. Gopinathan, K. C. Huang and D. B. Weibel, *Mol. Microbiol.*, 2012, **84**, 874.
13 E. R. Rojas, G. Billings, P. D. Odermatt, G. K. Auer, L. Zhu, A. Miguel, F. Chang, D. B. Weibel, J. A. Theriot and K. C. Huang, *Nature*, 2018, **559**, 617.
14 S. Al-Mosleh, A. Gopinathan, C. D. Santangelo, K. C. Huang and E. R. Rojas, *Proc. Natl. Acad. Sci. U. S. A.*, 2022, **119**(41), e2200728119.
15 E. R. Rojas and K. C. Huang, *Curr. Opin. Microbiol.*, 2018, **42**, 62.
16 G. K. Auer, T. K. Lee, M. Rajendram, S. Cesar, A. Miguel, K. C. Huang and D. B. Weibel, *Cell Syst.*, 2016, **2**, 402.
17 G. K. Auer and D. B. Weibel, *Biochemistry*, 2017, **56**, 3710.
18 P. N. Rather, *Environ. Microbiol.*, 2005, **7**, 1065.
19 M. F. Copeland and D. B. Weibel, *Soft Matter*, 2009, **5**, 1174.
20 G. K. Auer, P. M. Oliver, M. Rajendram, T.-Y. Lin, Q. Yao, G. J. Jensen and D. B. Weibel, *mBio*, 2019, **10**, e00210.

21 G. K. Auer, P. M. Oliver, M. Rajendram, T.-Y. Lin, Q. Yao, G. J. Jensen and D. B. Weibel, *mBio*, 2019, **10**, e00210.

22 R. R. Trivedi, J. A. Crooks, G. K. Auer, J. Pendry, I. P. Foik, A. Siryaporn, N. L. Abbott, Z. Gitai and D. B. Weibel, *mBio*, 2018, **9**, e01340.

23 D. B. Kearns, *Nat. Rev. Microbiol.*, 2010, **8**, 634.

24 H. H. Tuson, M. F. Copeland, S. Carey, R. Sacotte and D. B. Weibel, *J. Bacteriol.*, 2013, **195**, 368.

25 J. Blake, *J. Fluid Mech.*, 1972, **55**, 1.

26 C. Brennen and H. Winet, *Annu. Rev. Fluid Mech.*, 1977, **9**, 339.

27 J. F. M. Hoeniger, *Microbiol.*, 1965, **40**, 29.

28 E. Lauga, *The fluid dynamics of cell motility*, 62, Cambridge University Press, 2020.

29 O. Du Roure, A. Lindner, E. N. Nazockdast and M. J. Shelley, *Annu. Rev. Fluid Mech.*, 2019, **51**, 539.

30 A. Lindner and M. Shelley, *Fluid-structure interactions in low-Reynolds-number flows*, 2015, vol. 168.

31 L. Li, H. Manikantan, D. Saintillan and S. E. Spagnolie, *J. Fluid Mech.*, 2013, **735**, 705.

32 J. T. Pham, A. Morozov, A. J. Crosby, A. Lindner and O. du Roure, *Phys. Rev. E: Stat., Nonlinear, Soft Matter Phys.*, 2015, **92**, 011004(R).

33 H. Manikantan and D. Saintillan, *Phys. Rev. E: Stat., Non-linear, Soft Matter Phys.*, 2015, **92**, 041002(R).

34 Y. Liu, B. Chakrabarti, D. Saintillan, A. Lindner and O. Du Roure, *Proc. Natl. Acad. Sci. U. S. A.*, 2018, **115**, 9438.

35 B. Chakrabarti, Y. Liu, J. LaGrone, R. Cortez, L. Fauci, O. du Roure, D. Saintillan and A. Lindner, *Nat. Phys.*, 2020, **16**, 689.

36 C. Floyd, H. Ni, R. S. Gunaratne, R. Erban and G. A. Papoian, *J. Chem. Theory Comput.*, 2022, **18**, 4865.

37 G. Jayaraman, S. Ramachandran, S. Ghose, A. Laskar, M. S. Bhamla, P. S. Kumar and R. Adhikari, *Phys. Rev. Lett.*, 2012, **109**, 158302.

38 F. Ling, H. Guo and E. Kanso, *J. R. Soc., Interface*, 2018, **15**, 20180594.

39 X. Shi, A.-K. Pumm, J. Isensee, W. Zhao, D. Verschueren, A. Martin-Gonzalez, R. Golestanian, H. Dietz and C. Dekker, *Nat. Phys.*, 2022, **18**, 1105.

40 A. Laskar and R. Adhikari, *Soft Matter*, 2015, **11**, 9073.

41 R. E. Isele-Holder, J. Elgeti and G. Gompper, *Soft Matter*, 2015, **11**, 7181.

42 R. G. Winkler, J. Elgeti and G. Gompper, *J. Phys. Soc. Jpn.*, 2017, **86**, 101014.

43 Y. Man and E. Kanso, *Soft Matter*, 2019, **15**, 5163.

44 A. Ghosh and N. Gov, *Biophys. J.*, 2014, **107**, 1065.

45 D. Saintillan, M. J. Shelley and A. Zidovska, *Proc. Natl. Acad. Sci. U. S. A.*, 2018, **115**, 11442.

46 C. W. Wolgemuth, T. R. Powers and R. E. Goldstein, *Phys. Rev. Lett.*, 2000, **84**, 1623.

47 S. Lim and C. S. Peskin, *SIAM J. Sci. Comput.*, 2004, **25**, 2066.

48 T. R. Powers, *Rev. Mod. Phys.*, 2010, **82**, 1607.

49 R. E. Goldstein, T. R. Powers and C. H. Wiggins, *Phys. Rev. Lett.*, 1998, **80**, 5232.

50 A. Goriely and M. Tabor, *Physica D*, 1997, **105**, 45.

51 A. Goriely and M. Tabor, *Physica D*, 1997, **105**, 20.

52 M. Nizette and A. Goriely, *J. Math. Phys.*, 1999, **40**, 2830.

53 F. Gay-Balmaz, D. D. Holm and T. S. Ratiu, *J. Geom. Mech.*, 2009, **1**, 417.

54 F. Boyer and F. Renda, *J. Nonlinear Sci.*, 2017, **27**, 1.

55 D. C. Ellis, F. Gay-Balmaz, D. D. Holm and T. Ratiu, *J. Geom. Phys.*, 2011, **61**, 2120.

56 G. K. Auer, P. M. Oliver, M. Rajendram, T.-Y. Lin, Q. Yao, G. J. Jensen and D. B. Weibel, *mBio*, 2019, **10**(5), e00210–19.

57 S. S. Antman, *Nonlinear Problems of Elasticity*, Springer, 1995.

58 A. Shapere and F. Wilczek, *J. Fluid Mech.*, 1989, **198**, 557.

59 R. W. R. Darling, *Differential Forms and Connections*, Cambridge University Press, 1994.

60 A. Iserles, H. Z. Munthe-Kaas, S. P. Nørsett and A. Zanna, *Acta Numer.*, 2000, **9**, 215.

61 G. G. Giusteri and E. Fried, *J. Elast.*, 2018, **132**, 43.

62 J. Park and W.-K. Chung, *IEEE Trans. Robot.*, 2005, **21**, 850.

63 E. Haier, C. Lubich and G. Wanner, *Geometric Numerical Integration: Structure-Preserving Algorithms for Ordinary Differential Equations*, Springer, 2006.

64 P. E. Crouch and R. Grossman, *J. Nonlinear Sci.*, 1993, **3**, 1.

65 H. Wada, *Phys. Rev. E: Stat., Nonlinear, Soft Matter Phys.*, 2011, **84**, 042901.

66 E. Lauga and T. Powers, *Rep. Prog. Phys.*, 2009, **72**, 096601.

67 A. Iserles and S. P. Nørsett, *Philos. Trans. R. Soc., A*, 1999, **357**, 983.

68 S. Blanes, F. Casas, J.-A. Oteo and J. Ros, *Phys. Rep.*, 2009, **470**, 151.

69 S. Lim, *Phys. Fluids*, 2010, **22**, 024104.

70 B. E. Griffith and S. Lim, *Comm. Comput. Phys.*, 2012, **12**, 433.

71 S. D. Olson, S. Lim and R. Cortez, *J. Comput. Phys.*, 2013, **238**, 169.

72 W. Lee, Y. Kim, S. D. Olson and S. Lim, *Phys. Rev. E: Stat., Nonlinear, Soft Matter Phys.*, 2014, **90**, 033012.

73 L. Koens and E. Lauga, *Phys. Fluids*, 2016, **28**, 013101.

74 O. Maxian, B. Sprinkle, C. S. Peskin and A. Donev, *Phys. Rev. Fluids*, 2022, **7**, 074101.

75 B. J. Walker, K. Ishimoto and E. A. Gaffney, *Phys. Rev. Fluids*, 2023, **8**(3), 034101.

76 M. Garg and A. Kumar, *Math. Mech. Solids*, 2023, **28**, 692.

77 Y. L. Lin, N. J. Derr and C. H. Rycroft, *Proc. Natl. Acad. Sci. U. S. A.*, 2022, **119**, e2105338118.

78 O. Maxian and A. Donev, *J. Fluid Mech.*, 2022, **952**, A5.

79 C. H. Wiggins, D. Riveline, A. Ott and R. E. Goldstein, *Biophys. J.*, 1998, **74**, 1043.

80 D. Lovelock and H. Rund, *Tensors, Differential Forms, and Variational Principles*, Courier Corporation, 1989.